



Structure dependency of the atomic-scale mechanisms of platinum electro-oxidation and dissolution

Timo Fuchs¹, Jakub Drnec², Federico Calle-Vallejo³, Natalie Stubb⁴, Daniel J. S. Sandbeck^{5,6}, Martin Ruge¹, Serhiy Cherevko⁵, David A. Harrington⁴ and Olaf M. Magnussen¹✉

Platinum dissolution and restructuring due to surface oxidation are primary degradation mechanisms that limit the lifetime of platinum-based electrocatalysts for electrochemical energy conversion. Here, we have studied well-defined Pt(100) and Pt(111) electrode surfaces by in situ high-energy surface X-ray diffraction, online inductively coupled plasma mass spectrometry and density functional theory calculations to elucidate the atomic-scale mechanisms of these processes. The locations of the extracted platinum atoms after Pt(100) oxidation reveal distinct differences from the Pt(111) case, which explains the different surface stability. The evolution of a specific oxide stripe structure on Pt(100) produces unstable surface atoms that are prone to dissolution and restructuring, leading to one order of magnitude higher dissolution rates.

The degradation of Pt catalysts in the cathode reaction in fuel cells is linked to their electro-oxidation and dissolution¹.

Both these processes are arguably even more complex than the actual energy conversion by oxygen reduction and have been studied for a long time, mainly in polycrystalline and supported nanoparticle catalysts. Now, single-crystal studies offer the prospect of a more detailed understanding of these processes at the atomic level^{2–11}. Previously, some studies followed these processes by potential cycling, and it is known that surface restructuring over many cycles leads to a roughened surface and that dissolution is enhanced during oxide reduction^{12–22}. Explanations of this behaviour generally invoke a place exchange (PE) process, in which a Pt surface atom leaves its lattice site and oxygen penetrates into the metal lattice. On Pt(111), pioneering studies demonstrated that PE can be directly observed by surface X-ray diffraction (SXRD)^{4,5}. More recent SXRD measurements confirmed this^{18,23–25} and allowed structural refinement, showing that the exchanged Pt atom lies 2.4 Å above its original lattice site¹⁸, in good agreement with density functional theory (DFT) studies of this process^{26–28}. In contrast to Pt(111), other Pt crystal faces show distinct differences in their oxidation and dissolution behaviour^{10,12,14,29}. This has been qualitatively explained by the more open arrangement of the surface atoms, but precise atomic-level data are scarce. Thus, clear structure–reactivity relationships, which for example would guide the development of tailored Pt catalysts, are still lacking.

We here present the results of detailed structural studies, focusing on the precise atomic motions in the early stages of oxidation. By correlating in situ SXRD measurements, which reveal how the place-exchanged Pt atoms are arranged in the initial stages of surface oxidation, with detailed DFT calculations of this process, a direct comparison of the elementary processes underlying Pt(111) and Pt(100) oxidation becomes possible. Our study reveals a sharply

different mechanism for the oxidative extraction of Pt atoms out of the two surfaces, providing a detailed explanation for the enhanced dissolution on Pt(100) observed by online mass spectrometry.

Results

Dissolution and surface restructuring by electro-oxidation.

According to cyclic voltammetry studies, the onset of Pt oxidation on the Pt(111) and Pt(100) surfaces is marked by a current peak above 1.0 V (labelled O_{ads} in Fig. 1b,c and Extended Data Fig. 1). However, the cyclic voltammograms (CVs) of Pt(100) show irreversible changes in subsequent cycles, whereas those of Pt(111) remain stable for an upper potential limit (UPL) of $\lesssim 1.15$ V and thus can be mistaken for an oxidation process without surface restructuring^{7,12,29}.

The (ir)reversibility of the CVs is mirrored in the Pt dissolution rates obtained by inductively coupled plasma mass spectrometry (ICP-MS) in a (capillary) scanning flow cell (denoted CSFC-ICP-MS and SFC-ICP-MS, respectively) with the results summarized in Fig. 1a,d. The facet-dependent trends are readily apparent. At sweep rates of $\gtrsim 10$ mV s⁻¹, no dissolution is seen for either surface for CVs with a UPL of 1.0 V, in agreement with previous results^{14,16}. On increasing the UPL, the onset of substantial anodic dissolution (relative to detection limits) due to Pt oxidation is observed for Pt(100) as soon as the O_{ads} peak begins, whereas for Pt(111) the onset only occurs at potentials above 1.2 V. Cathodic dissolution during the oxide reduction is observed for both surfaces at UPLs ≥ 1.1 V; however, the dissolution of Pt(100) exceeds that of Pt(111) by about one order of magnitude. The onset and amount of dissolution depend on the precise time–potential program, reflecting the slow oxidation kinetics¹⁴; however, enhanced rates were found for Pt(100) as compared with Pt(111) in all experiments. It is noted that the amount of oxide formed in both cases is

¹Institut für Experimentelle und Angewandte Physik, Christian-Albrechts-Universität zu Kiel, Kiel, Germany. ²Experimental Division, European Synchrotron Radiation Facility, Grenoble, France. ³Departament de Ciència de Materials i Química Física & Institut de Química Teòrica i Computacional (IQTCUB), Universitat de Barcelona, Barcelona, Spain. ⁴Chemistry Department, University of Victoria, Victoria, British Columbia, Canada. ⁵Helmholtz-Institute Erlangen-Nürnberg for Renewable Energy (IEK-11), Forschungszentrum Jülich, Erlangen, Germany. ⁶Department of Chemical and Biological Engineering, Friedrich-Alexander-Universität Erlangen-Nürnberg, Erlangen, Germany. ✉e-mail: magnussen@email.uni-kiel.de

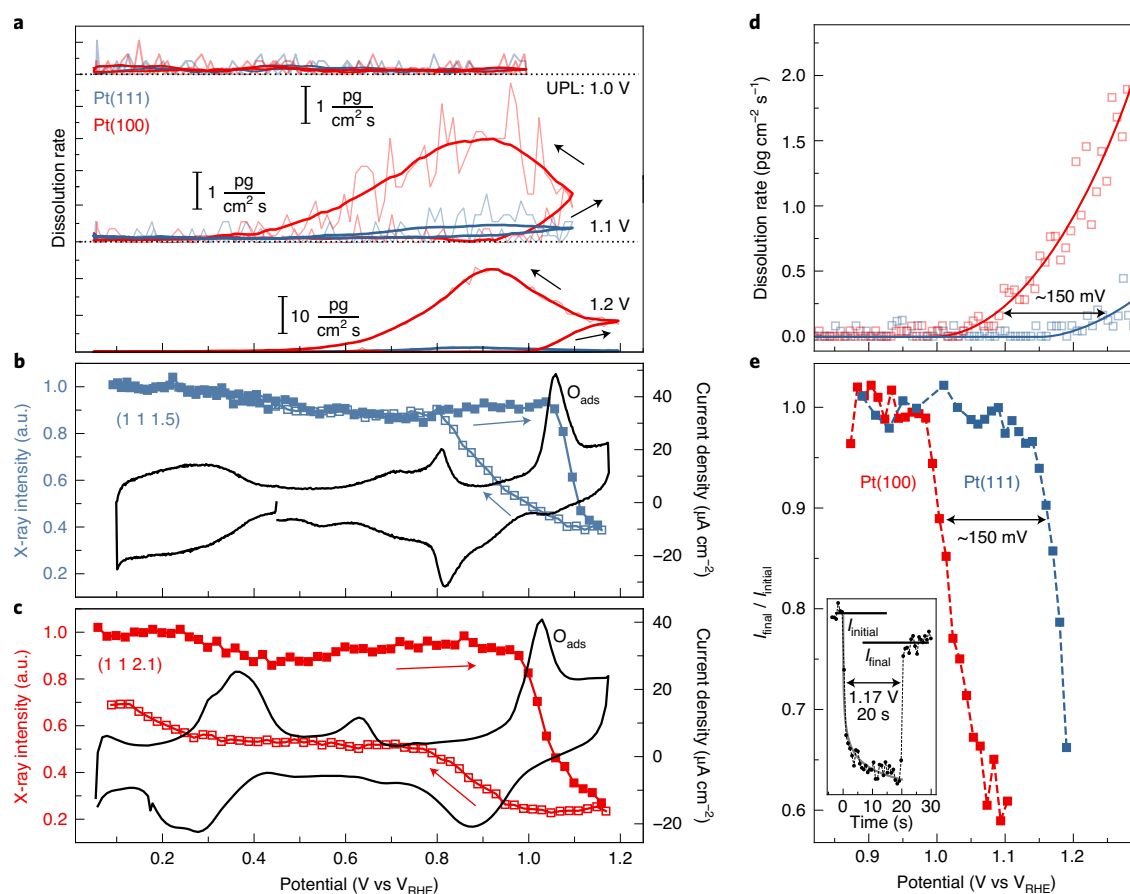


Fig. 1 | Dissolution and atomic-scale structural changes during Pt oxidation. **a**, Pt dissolution during cycles at 50 mV s⁻¹ at UPLs of 1, 1.1 and 1.2 V, obtained using a capillary scanning flow cell, illustrating that cathodic dissolution during oxide reduction is considerably more pronounced on Pt(100) than on Pt(111). RHE, reversible hydrogen electrode. **b,c**, Changes in X-ray intensity at the anti-Bragg positions of selected CTRs ((1 1 1.5) on Pt(111) and (1 1 2.1) on Pt(100), squares) and simultaneously measured CVs (black lines) of Pt(111) (**b**, data taken from ref. ²³) and Pt(100) (**c**) during potential cycles at 20 mV s⁻¹. Filled and empty squares indicate the X-ray intensity during the forward and reverse potential sweep, respectively. Pt PE, indicated by the intensity drop at the O_{ads} peak, is initially fully reversible on Pt(111), whereas for Pt(100) it always results in irreversible surface restructuring. **d**, Potential-dependent Pt dissolution rates for Pt(111) and Pt(100) during a positive sweep at 10 mV s⁻¹, obtained with a scanning flow cell, showing the onset of anodic dissolution. **e**, Reversibility of the PE process for Pt(111) and Pt(100), determined by potential step experiments, in which the potential was changed from 0.47 V in the double layer range to a potential in the oxidation regime for 20 s and then returned to 0.47 V (as an example, a potential step to 1.17 V is shown in the inset). The relative changes in X-ray intensity indicate that irreversible Pt surface restructuring starts on Pt(111) at a potential ~150 mV higher than on Pt(100).

comparable, only about 20% higher for Pt(100) (as seen from the integral of the oxidation peaks in the CVs). Thus, the large difference in dissolution rates points towards a fundamentally different oxidation behaviour of the two surfaces. Similar facet-dependent trends have been found in previous comparative studies of the dissolution behaviour of Pt(100) and Pt(111)^{14,16}, but these studies did not link the difference to the oxide structure nor provide mechanistic explanations due to the lack of knowledge of structural changes during surface oxidation.

The atomic-scale origin of this difference was investigated by in situ SXR. This technique determines the exact positions of surface atoms during the initial stages of oxidation, which can then be linked to the dissolution and surface restructuring mechanisms. For a qualitative assessment of the influence of surface orientation, we first followed the reflections near the anti-Bragg positions of the crystal truncation rods (CTRs). These are sensitive to the distortion of the ideal Pt lattice and the extraction of Pt atoms out of the surface in the PE process^{4,5,23}. Performing such measurements during potential cycles revealed that on both surfaces the onset of PE coincides with the O_{ads} peak maximum (0.98 and 1.04 V on Pt(100) and Pt(111), respectively), but that the subsequent structural response

is very different (Fig. 1b,c). PE on Pt(100) results in irreversible surface structural changes, as indicated by the irreversible decrease in X-ray intensity after completion of one potential cycle. In contrast, the PE process on Pt(111) is initially fully reversible^{4,23} and only results in irreversible surface restructuring if the UPL exceeds 1.15 V. Here, the onset of irreversibility occurs above a critical coverage of extracted Pt atoms²³, which depends on the potential and time in the oxidation regime. A more quantitative comparison of the onset of irreversible intensity changes, obtained in potential step experiments (Fig. 1e), indicates that these occur on Pt(111) at potentials about 150 mV more positive than on Pt(100), closely mirroring the onset of Pt dissolution (Fig. 1d). This unambiguously demonstrates that dissolution and irreversible surface structural changes on single-crystal surfaces are linked. Lopes et al.^{14,15} have previously stated the latter observation and associated it with the oxide peak around 1 V, but in this work the onset of irreversibility is clearly defined by the X-ray data (Fig. 1e), and in the case of Pt(111) is after the oxide peak. Furthermore, our observations resemble the findings of Huang et al.¹⁰, who reported that in situ Raman spectroscopy bands associated with the formation of the three-dimensional α-PtO₂ oxide phase occur at potentials 200 mV

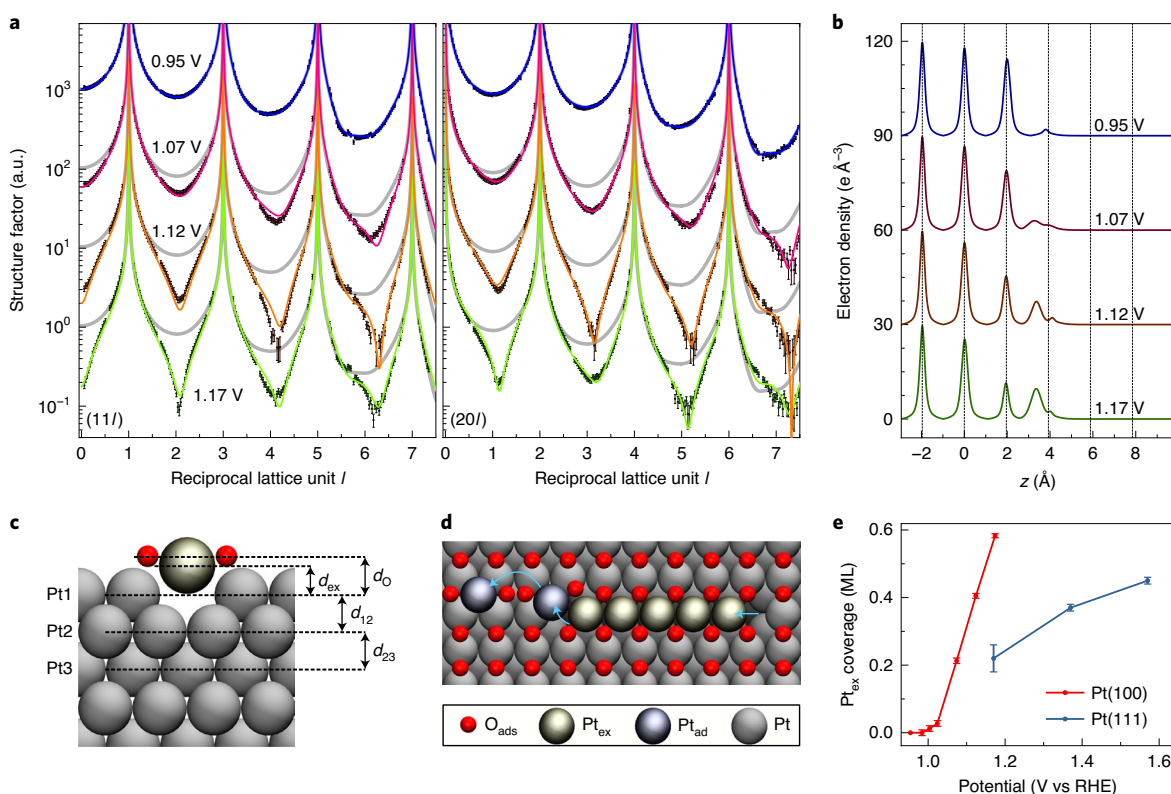


Fig. 2 | Atomic structure of the PE site on Pt(100). **a**, Two of the 11 measured CTRs of Pt(100), obtained by in situ HESXRD measurements (68 keV) at one potential slightly negative (0.95 V) and three potentials positive (1.07, 1.12 and 1.17 V) with respect to the O_{ads} peak in the CV (Fig. 1b and Extended Data Fig. 1). The curves positive to the O_{ads} peak exhibit considerably decreased intensities and correspond to surfaces in which 20–60% of the Pt atoms have undergone PE. Each set of CTRs was recorded within 550 s, starting 300 s after the potential was established. The full CTR data sets are given in Extended Data Fig. 3. In addition to the experimental data (black dots), which are offset by a factor of ten with respect to each other, the best fits (coloured lines) and the CTR fits (grey line) for the smooth surface at 0.95 V are shown. **b**, Electron density profiles along the surface normal z on Pt(100), obtained from quantitative modelling of the CTRs. The bulk Pt lattice positions are indicated by dashed vertical lines. **c, d**, Side (**c**) and top (**d**) views of the atomic arrangement of Pt atoms extracted out of Pt(100). The labels in **c** correspond to the vertical spacing parameters d , which have been used in the CTR fits. All structural parameters and the parameter values obtained in the CTR fits are listed in Supplementary Table 2. The symbols defining atom types in **d** also relate to **c**. **e**, Potential-dependent Pt_{ex} coverage on Pt(100), obtained from the CTR analysis, and compared with the Pt_{ex} coverage on Pt(111) (taken from ref. ¹⁵). The error bars represent standard deviations calculated using the covariance method. Further details of the analysis of the uncertainties are given in the Methods.

more negative on Pt(100) than on Pt(111). However, PE on Pt(111) was here proposed to occur only at ≥ 1.3 V, which is at variance with the SXRD results. Therefore, a clear correlation between the precise oxide structure of different Pt surfaces, its reversibility and its effect on dissolution is still lacking.

Atomic-scale structure of the Pt oxide. To assess the difference between the reversible and irreversible structural processes, we performed a detailed potential-dependent surface crystallographic analysis on an extended set of CTRs. An overview of all the measured data sets is given in Supplementary Note 1. For Pt(111), the arrangement of surface atoms was determined in our previous study^{18,23}. At low coverage, PE was found to result in a vertical displacement of the extracted Pt atom (Pt_{ex}) of only ~ 2 Å, with the in-plane position remaining the same. Thus, Pt_{ex} is located directly above its original site, which is either vacated or filled with oxygen. Previous DFT studies also found this unusual geometry and indicated that it is stabilized by three neighbouring oxygen adsorbate atoms on the Pt(111) surface²⁷.

Similar structural characterization of the initial stages of Pt(100) oxidation is more difficult, because, unlike on Pt(111), the surface oxide continuously evolves over a period of hours. This strongly impedes the use of conventional SXRD measurements, which typically require a recording time of 1–2 h. We therefore performed

in situ measurements using the novel technique of high-energy surface X-ray diffraction (HESXRD)³⁰, which allows the collection of data from many CTRs in just a few minutes, that is, in a period of time in which the structural changes in the oxide are negligible.

The CTRs measured on Pt(100) at 0.12 V are shown in Extended Data Fig. 2 (see Supplementary Fig. 2 and Supplementary Note 2 for further details of the CTR analysis) and examples of the 11 CTRs measured at each of the potentials 0.95, 1.07 and 1.12 V are shown in Fig. 2a (see Extended Data Fig. 3 for the full data set). The measurements at 0.12 V confirmed that the initial surface is unreconstructed and exhibits negligible roughness. At potentials slightly negative with respect to the O_{ads} peak in the CV (0.95 V), the adsorption of oxygen species is signalled by changes in the Pt surface relaxation and increased statistical deviations of the Pt surface atoms from ideal lattice positions, characterized by larger Debye–Waller factors. After the onset of PE (≥ 1.07 V), the intensity of all CTRs substantially decreases. This change cannot be described by Pt_{ex} in an on-top geometry, as in the case of Pt(111), or in conventional hollow or bridge sites atop the Pt surface (see Supplementary Note 3 for details of the data analysis). A good description of the large HESXRD data sets was only possible using models that assume that the majority of extracted Pt atoms reside in bridge sites with vertical positions that are merely 1.40 Å (d_{ex} in Fig. 2c) above the Pt(100) surface plane (see Fig. 2b for the electron density along the

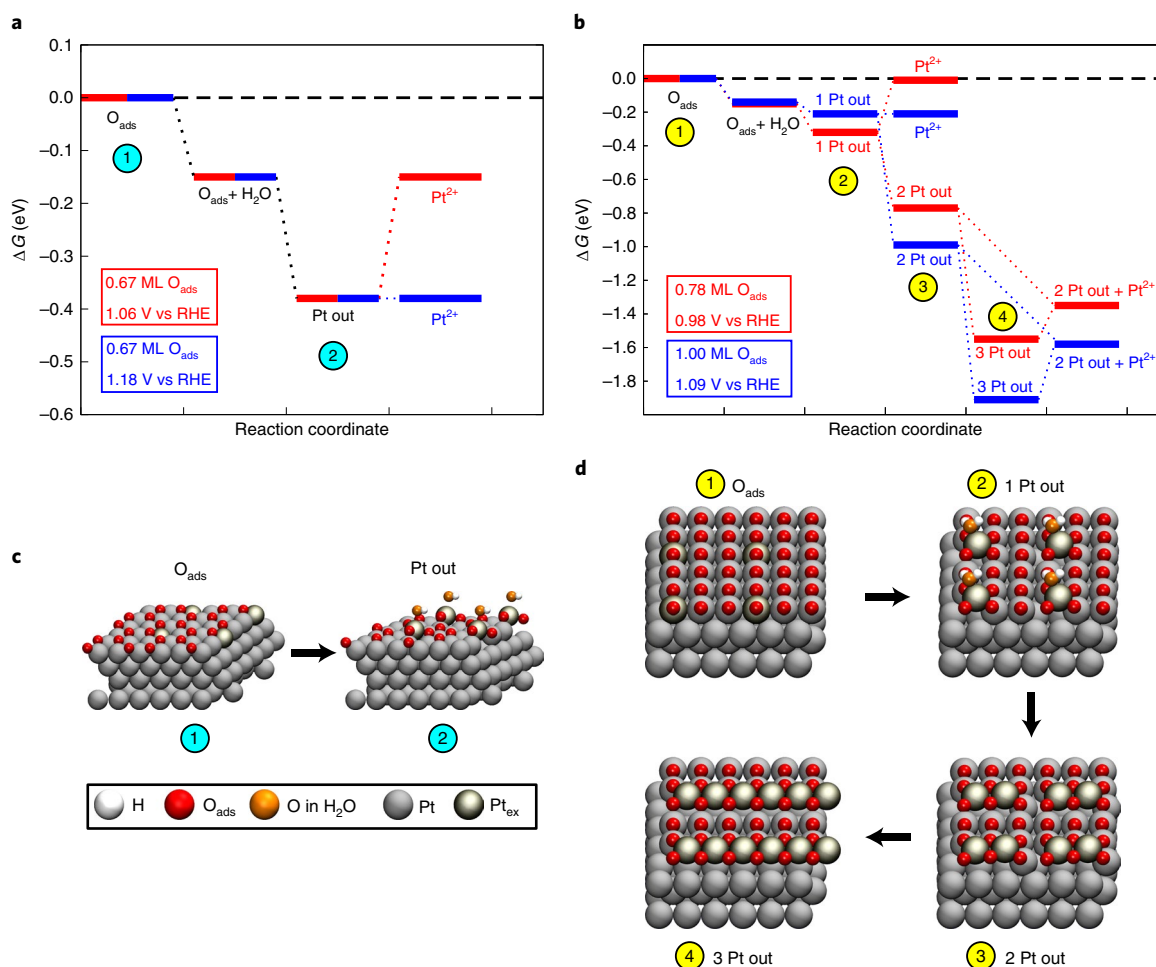


Fig. 3 | Atomistic view of PE and dissolution on Pt(111) and Pt(100). **a, b**, Free-energy landscapes of PE and dissolution obtained from DFT calculations of Pt(111) (**a**) and Pt(100) (**b**). **c, d**, Corresponding schematics of the main steps in the reaction pathways for PE and dissolution on Pt(111) (**c**) and Pt(100) (**d**). The symbols defining atom types in **c** also relate to **d**. In both cases, surface wetting by H₂O is accounted for and observed to aid the extraction process (for clarity, H₂O is not shown in steps 3 and 4 of **d**). Dissolution of the first Pt_{ex} in the form of Pt²⁺ is not favoured at low potentials (1.06 V on Pt(111), 0.98 V on Pt(100)), but becomes energetically favourable at higher potentials (1.18 V on Pt(111), 1.09 V on Pt(100)). Further Pt extraction proceeds differently on Pt(100), from which a second and third extraction are favourable, leading to an extended stripe of extracted Pt atoms. Parallel to the stripe extraction process, dissolution can occur at 0.98 V by detachment of one of the Pt atoms in the dimer formed after the second stripe extraction. Top and side views of the surfaces are provided in Extended Data Fig. 6.

surface normal obtained from the CTR fits). These models allowed all the CTR data obtained at different oxidation potentials to be fitted with very similar structure parameters, apart from the Pt_{ex} coverage, which continuously increased up to 0.6 monolayers (ML) with increasing potential (Fig. 2e, see Supplementary Table 2 for all structural parameters). We note that the Pt_{ex} coverage on Pt(111) increases more moderately, to 0.45 ML at 1.57 V (ref. 18).

The low vertical position of Pt_{ex} is sterically incompatible with species residing atop the surface, but can be readily explained by Pt atoms that are bound through surface or subsurface oxygen to the centre of a vacancy dimer. The resulting geometry distinctly differs from that of Pt_{ex} on Pt(111), both in terms of the coordination as well as the distances of Pt_{ex} to the neighbouring atoms in the Pt surface layer (~0.2 Å longer) and the vertical spacing of Pt_{ex} to the layer below ($d_{\text{ex}} > 2.23$ Å (ref. 18) on Pt(111), $d_{\text{ex}} < 1.42$ Å on Pt(100)). The formation of such a vacancy dimer requires extraction of a second Pt atom from the surface layer (Pt_{ad}), which can be positioned as an adatom on the surrounding Pt surface or as a slightly more protruding atom at the end of the dimer. However, Pt_{ex} and Pt_{ad} are not necessarily generated in equal numbers. For example,

only one additional Pt_{ad} would be produced in the growth of a Pt oxide chain structure (Fig. 2d), similarly to those found in scanning tunnelling microscopy studies^{31,32} and DFT calculations²⁶ of Pt(111) oxidation in the gas phase. In this case, Pt_{ad} would only be formed as a minor species, not necessarily detectable in SXRD experiments. Indirect support for this scenario comes from the CTR data obtained at 0.12 V after oxide reduction, which are presented in Extended Data Fig. 2. Here, Pt_{ad} is clearly present in hollow sites, but at coverages that are ten times lower than that of Pt_{ex} in the corresponding oxide film. This also suggests that on Pt(100) the majority of Pt_{ex} directly return to the surface vacancies after reduction.

Mechanism of oxide formation and Pt dissolution. To further confirm the proposed structural evolution, we performed a comparative DFT study of the PE and Pt dissolution processes. We first calculated the Pourbaix diagrams for Pt(111) and Pt(100) (Extended Data Fig. 5) to determine the most stable oxygen coverage and adsorption sites as a function of pH and applied potential. The stabilization granted by water wetting was taken into account

in the free-energy assessment of all species (see the Methods for further details).

In good agreement with the experimental data (Fig. 1b,c), platinum extraction was calculated to be thermodynamically favourable from 1.06 V at oxygen coverage $\theta_{\text{O}} \approx 0.67$ ML on Pt(111) and from ≥ 0.98 V at $\theta_{\text{O}} \approx 0.78$ ML for Pt(100) (Extended Data Fig. 4). According to the energy calculations of the various steps in the PE process (Fig. 3a,b), PE starts on Pt(111) with O_{ads} adsorption (Fig. 3, step 1) followed by the extraction of a Pt atom (step 2). In line with previous SXRD^{18,23} and DFT²⁷ studies, the extracted Pt atom is located above a vacancy and coordinated to three O_{ads} atoms (Fig. 3c and Extended Data Fig. 6).

Our extraction pathway on Pt(111) is similar to the one reported by Eslamibidgoli and Eikerling²⁷, who found that PE starts at oxygen coverages between 0.59 and 0.75 ML. The pathway for PE on Pt(100) is substantially different from that on Pt(111) (Fig. 3b). Although it also starts by O_{ads} adsorption and the extraction of a Pt atom, the high O_{ads} coverage allows Pt extraction to proceed immediately at neighbouring sites. Hence, consecutive extraction of Pt atoms occurs that ultimately leads to the creation of a stripe of protruding atoms. In agreement with our experiments, the Pt_{ex} atoms are not located above their original lattice sites, but move sideways to a square-planar site where they are coordinated by four O_{ads} atoms. This fourfold oxygen coordination strongly stabilizes the structure, contrary to the case of Pt(111), where stripe-like structures lead to only small gains in free energy as compared with isolated Pt_{ex} ²⁶. The greater O_{ads} coordination around Pt_{ex} may lead to the Raman signature resembling that of PtO_2 , as previously observed for Pt(100) in this potential range¹⁰. Furthermore, we note that the first Pt_{ex} of each stripe deviates from the perfect square-planar site for steric reasons (see the Pt_{ex} positions after the first and second extraction in Fig. 3d), resulting in the more weakly bound Pt_{ad} species postulated above.

The differences in the anodic dissolution of Pt(111) and Pt(100) upon oxidation, that is, the conversion of Pt_{ex} into a Pt ion (assumed to be Pt^{2+})³³, can be ascribed to the different Pt extraction processes. On Pt(111), the Pt_{ex} atoms are initially arranged directly above the vacancy, and this is thermodynamically more stable than a Pt^{2+} -vacancy pair (see Fig. 3a and the Methods). Only after the potential is increased to 1.18 V does the dissolution become energetically favourable (Fig. 3a and Extended Data Fig. 4). The situation is different for Pt(100) (Fig. 3b), where dissolution is not favoured at 0.98 V during the first extraction; however, the atomic arrangement formed after the second extraction is prone to dissolution. The DFT calculations showed this process to be exothermic and its final state is the same as when three Pt atoms are extracted and one of them dissolves (two Pt out + Pt^{2+} in Fig. 3b). The reason for this is that a further Pt surface atom is subsequently extracted following dissolution from the second extraction state. This leads to stabilization of the system, because the dimer formed is now better positioned in the triple vacancy. Thus, the Pt_{ex} atoms formed in the initial stages of stripe formation as well as the more weakly bound Pt_{ad} at the ends of stripes are prone to dissolution. This explains the higher anodic dissolution rates and lower dissolution potentials of Pt(100) as compared with Pt(111), where no similar destabilized atoms exist. When the potential exceeds that for 1 ML O_{ads} coverage (1.09 V), dissolution can also take place during the first extraction step.

The initial reversibility of the PE process and stability against cathodic dissolution on Pt(111) can be attributed to the on-top arrangement found in our SXRD and DFT studies, when the Pt_{ex} coverage is low and the Pt(111) lattice around the vacancy on which O_{ads} atoms are adsorbed remains intact. This on-top geometry facilitates the back insertion of Pt_{ex} into the vacancy after the desorption of oxygen in the reduction process ($\Delta G_{\text{ex}} = -0.5$ eV at $\theta_{\text{O}} = 0.44$ ML, Extended Data Fig. 4) rather than the formation of a Pt adatom-vacancy pair by detachment or dissolution in the form of Pt^{2+} , as

discussed in a previous report¹⁵. At higher Pt_{ex} coverage, the oxide surface structure is more complex, impeding straightforward conclusions on the exact restructuring process. However, the increasing deviations of Pt_{ex} from the on-top positions, observed by SXRD¹⁸, suggest a gradual loss in the overall integrity of the Pt surface lattice, which may account for the irreversible surface roughening during subsequent oxide reduction as well as the Pt cathodic dissolution.

By contrast, on Pt(100), we expect Pt adatoms and Pt^{2+} formation directly at the ends of the Pt_{ex} stripes during oxidation. Similarly, Pt adatoms and Pt^{2+} are also expected to form during oxide reduction as the O_{ads} coverage decreases. As the stripes shorten, the remaining destabilized Pt_{ad} atoms at the ends of the stripes are more likely to dissolve or form adatoms.

Conclusion

The onset potentials for anodic dissolution on Pt(100) and Pt(111) correspond to the onset of irreversibility in the extraction of the first Pt atoms from their lattice sites as the surface is oxidized. According to our combined SXRD and DFT studies, the marked difference in behaviour of the two surfaces has its origin in the different atomic structures of the initial oxide. On Pt(111), the extracted Pt atom lies directly above its original site, and the reversibility at low coverage is explained by its facile return to that site. However, on Pt(100), the extracted Pt atom moves laterally away from its original site and initiates the immediate extraction of a second atom, leading to the formation of a stripe structure. This mechanism produces unstable surface atoms at stripe ends that can dissolve both during the oxidation itself and during the subsequent oxide reduction, making the process irreversible from its onset.

As shown by our data, the precise mechanisms of Pt extraction during oxidation and the accompanying dissolution differ substantially on different Pt facets. This sensitivity of Pt electrocatalyst degradation to surface structure has to be taken into account in the quest for a knowledge-based approach to catalyst design, where highly stable catalysts are ideally predicted by ab initio methods. Although our study represents the first step in developing an atomistic picture of these processes for surfaces other than Pt(111) (which may be considered as an atypical case according to the results presented here), further studies are necessary, especially of more open high-index surfaces. Such detailed insight into the degradation mechanisms of structurally defined model systems is an important prerequisite for the challenging task of ab initio modelling of the stability of real catalyst particles and, ultimately, developing rational strategies for the design of catalysts with improved stability.

Methods

Sample preparation. All experiments were performed using cylindrical Pt single crystals (Mateck, Crystal Preparation Laboratory) and argon-purged 0.1 M HClO_4 solution made from ultrapure water and Suprapur perchloric acid (Merck). Potentials were measured versus Ag/AgCl (saturated KCl for SFC-ICP-MS or 3.4 M KCl for SXRD) reference electrodes but are reported against the reversible hydrogen electrode. The Pt crystals were initially cleaned in an ultrahigh vacuum chamber by repeated Ar^+ bombardment and subsequent annealing at 900 °C in 10^{-6} mbar oxygen. Prior to each experiment, the Pt crystals were subjected to flame annealing with a butane torch (SFC-ICP-MS) or annealing under a 2:98 CO/Ar atmosphere in an induction oven (Himmelwerk HU-2000+, SXRD). Subsequently, the samples were cooled in a flow of 40:60 H_2/Ar (SFC-ICP-MS) or 2:98 CO/Ar (SXRD) and transferred to the cell protected either by a drop of argon-saturated ultrapure water or an adsorbed CO layer (SXRD, only Pt(100)). The samples were immersed in the electrolyte under potential control at potentials in the double layer regime. After immersion, the remaining adsorbed CO was removed by anodic stripping.

Dissolution measurements. Dissolution measurements at a low scan rate of 10 mV s^{-1} to resolve the onset potentials of dissolution were conducted using the classical SFC-ICP-MS technique (NexION 300X, Perkin Elmer). The working electrode had a contact area of 0.035 cm^2 . A graphite rod was used as the counter electrode and a double junction Ag/AgCl (Metrohm) as the reference electrode. In SFC-ICP-MS, ¹⁸⁷Re was used as the ICP-MS internal standard for platinum and a

flow rate of around $170 \mu\text{l min}^{-1}$ was used. The procedure used for the SFC-ICP-MS measurements has been reported in detail previously^{34,35}. The cyclic voltammetry experiments were carried out at relatively high scan rates using a modification of the SFC-ICP-MS technique, namely CSFC-ICP-MS, which allows for considerably increased time–potential resolution³⁶. By inserting a small capillary directly above the working electrode (Supplementary Fig. 9) and connecting directly to the ICP-MS by self-aspiration (bypassing the use of the peristaltic pump), delay times between the dissolution on the working electrode and ICP-MS detection can be reduced from around 25 to 3 s. Reduced delay times and shorter tubing distances limit the dispersion of dissolved species and therefore enhance the resolution of the dissolution rate profiles, for example, to clearly separate anodic and cathodic dissolution signals³⁷. The relatively high flow rate of $580 \mu\text{l min}^{-1}$ resulted in a collection efficiency >99%. Further details of this new technique can be found in ref. 38.

Electrochemical cell for surface X-ray diffraction. All SXRDX experiments employed the established SXRDX electrochemical cell, described in ref. 39. Inside this cell, the upward facing single-crystalline surface of the crystal sample forms a contact with the electrolyte through a free-standing meniscus. This geometry is similar to the hanging meniscus geometry commonly used in single-crystal electrochemistry and minimizes contributions from the defect-rich edges of the crystal. The amount of electrolyte inside the cell was controlled remotely using a motorized pump system with a precision of 1 μl . To prevent oxygen contamination, the meniscus was kept under an Ar atmosphere and the electrolyte reservoirs were continuously purged with Ar. We used a high-purity Pt foil with a surface area of about 120 mm^2 as counter electrode and a Ag/AgCl (3.4 M KCl, eDAQ) reference electrode. The reference electrode was connected through a micrometre-sized hole to a glass capillary, which was filled with 0.1 M HClO_4 and served as the Luggin capillary and salt bridge. This arrangement effectively ensured negligible leakage of KCl from the reference electrode to the cell. The cell and all glassware and tubing that were in contact with the electrolyte had previously been cleaned by soaking in a 4:1 mixture of concentrated H_2SO_4 and 30% H_2O_2 for at least 1 day. Afterwards, all materials were rinsed and boiled repeatedly in high-purity water (Elga purelab ultra 18.2 M Ω cm). The CVs of Pt(111) and Pt(100) in 0.1 M HClO_4 in the double layer potential region, prepared as described above and measured in the SXRDX electrochemical cell, are shown in Extended Data Fig. 1. For both surfaces, the voltammograms are in good agreement with those reported in the literature³⁹. CVs up to 0.6 V were recorded at the beginning of every SXRDX experiment to confirm that a high-quality surface had been obtained by the annealing process.

Surface X-ray diffraction setup. All SXRDX experiments were performed at undulator beamlines ID03 and ID31 of the European Synchrotron Radiation Facility using a six-circle geometry and a constant incident angle. A schematic illustration of the experimental setup is shown in Supplementary Fig. 6. The crystal inside the SXRDX cell was positioned with the surface facing upwards. Conventional SXRDX studies were performed at beamline ID03, focussing on kinetic studies of the Pt oxidation process by measuring the X-ray intensity at a fixed position along a CTR. Similarly to our previous studies^{17,18,23,24,40}, these measurements employed a photon energy of 22.5 keV, a (vertical/horizontal) beam size of $45 \times 750 \mu\text{m}^2$ and an angle of incidence of 0.3° . A small two-dimensional detector (Maxipix) mounted on the diffractometer arm was used to simultaneously measure the CTR and background intensities with a time resolution of 0.1 s. The structure factor of the CTR at the studied reciprocal space position was determined by first subtracting the background intensity and then taking the square root of the integrated diffraction rod intensity.

Operando HESXRDX measurements of the Pt(100) CTRs were performed at the high-energy beamline ID31 at a photon energy of 68 keV. To enhance the surface contribution, the incident angle was kept at 0.05° , which is below the critical angle of total external reflection. The beam size at the sample position was $12 \times 48 \mu\text{m}^2$. The orientation of the surface normal direction was aligned with a precision better than 0.005° relative to the in-plane rotation axis, to ensure that the angle of incidence did not change during sample rotation. The diffracted X-ray intensity was recorded with a stationary, large-area X-ray detector (Pilatus 2M CdTe), which was positioned 73 cm behind the sample. By this approach, a range of up to 12 \AA^{-1} momentum transfer perpendicular to the surface and a range of around $\pm 5.5 \text{ \AA}^{-1}$ momentum transfer parallel to the surface could be covered. The tilt angles between the detector plane and the incident beam direction were determined by recording the Debye–Scherrer rings of a CeO_2 powder calibration standard and analysing the data using the pyFAI software⁴¹. The reciprocal space coordinates for each detector pixel were calculated using the tilt-corrected angles. The positions of all visible Bragg reflections on the detector and the corresponding observed sample rotations were used to accurately determine the orientation of the crystal as described in the literature⁴². After mounting and alignment of the Pt sample, the positions of around 30 Bragg reflections from the bulk crystal were masked using small pieces of tungsten, placed directly in front of the two-dimensional detector. This was necessary to prevent damage to the detector by the intense Bragg reflections while measuring the weak CTR intensities with the unattenuated incident beam. The beamstops manifest as black areas on the detector frames (Supplementary Fig. 8 and missing data points in the CTR profiles). In addition,

the incident beam was blocked by a beamstop located about 10 cm behind the sample to reduce air scattering background.

Points in reciprocal space were described in terms of the Miller indices (hkl), where h and k correspond to reciprocal lattice unit cell vectors \mathbf{b}_1 and \mathbf{b}_2 in the surface plane and l to vector \mathbf{b}_3 along the surface normal. For Pt(100), we chose the conventional cubic reciprocal basis with lattice vectors $|\mathbf{b}_1| = |\mathbf{b}_2| = |\mathbf{b}_3| = 2\pi/a$, with $a = 3.9242 \text{ \AA}$ being the Pt lattice constant. In the case of Pt(111), we used a hexagonal unit cell with reciprocal lattice vectors of length $|\mathbf{b}_1| = |\mathbf{b}_2| = 8\pi/\sqrt{6}a$ and $|\mathbf{b}_3| = 2\pi/\sqrt{3}a$, which is common in SXRDX studies of face-centred cubic (fcc) (111) surfaces⁴³. Schematic illustrations of the reciprocal space geometries of Pt(111) and Pt(100) are shown in Supplementary Fig. 7. The Bragg reflections of Pt(111) are separated by $\Delta l_{\text{Bragg}} = 3$ and those of Pt(001) are separated by $\Delta l_{\text{Bragg}} = 2$ along the CTRs. The absence of some CTRs, such as (10 l) and (21 l) for Pt(100), is related to the chosen fcc unit cell.

Determination of the CTR structure factors. CTR data are commonly presented by plotting the structure factor F_{hkl} as a function of l . To determine structure factors by HESXRDX, the reciprocal space is mapped by continuously recording detector frames during a single rotation of the crystal around the surface normal³⁰. By summing all the detector frames recorded during reciprocal space mapping, the CTRs can be directly visualized (Supplementary Fig. 8, vertical lines). Because the unit cell of Pt(100) has a rotational symmetry of 90° , a 110° rotation was sufficient to collect all symmetrically non-equivalent CTRs. An angular resolution of 0.05° was chosen to achieve a high enough reciprocal space resolution for the low l values of the (31 l) CTR. The CTR structure factors were determined from these data using the BINoculars software⁴⁴. Here, the first correction factors for solid angle and polarization were applied to the measured intensities⁴⁵. Then, a three-dimensional representation of the reciprocal space was calculated by binning the intensities of each individual pixel, using the reciprocal space coordinates of each frame. For the analysis of the Pt(100) data, bin sizes of $\Delta h = 0.002$, $\Delta k = 0.002$ and $\Delta l = 0.03$ were used. This corresponds to a series of hk slices along the CTR separated by the distance Δl . Within this Δl range, the structure factor F_{hkl} of the CTR is assumed to be constant and was determined by taking the square root of the integrated X-ray intensity at the CTR position. The background intensity was integrated in a region close to the CTR position and subtracted from the CTR intensity. A more detailed description of the direct structure factor extraction in reciprocal space is given in the paper by Drnec et al.⁴⁶. To obtain the statistical uncertainties (σ_s) of each reflection, we extended the BINoculars software using a package that calculates these uncertainties according to Poisson statistics. The total number of measured reflections in each CTR data set was between 1,922 and 2,005. After averaging the symmetry equivalent reflections, between 802 and 808 reflections were available for the structural analysis. The agreement factor (ϵ) of the symmetry equivalent reflections was 0.08 ± 0.07 . The uncertainties of the averaged reflections (σ) were then calculated from $\sigma = \sqrt{\epsilon^2 F_{hkl}^2 + \sigma_s^2}$.

Fitting of structural models to the CTR data. To obtain the atomic positions of the surface atoms, all CTRs of a given data set were jointly fitted by a surface structural model using a Python-based software, developed by us for the quantitative analysis of HESXRDX data. Using this software, the structure factors, calculated from the model using kinematic scattering theory⁴⁷, were fitted to the experimentally observed structure factors by the least-squares method. Detailed descriptions of the analysis of the CTRs in the double layer region and in the region of oxide formation are given in Supplementary Notes 2 and 3, respectively. The statistical errors of the best-fit parameters given in Supplementary Tables 1–4 were calculated by the covariance matrix method⁴⁸. These errors only take into account the goodness of fit and the experimental errors of the observed reflections, which are given by the counting statistics and the agreement factor between symmetry equivalent reflections. Systematic errors due to the chosen fit model are not included here. These can be estimated from Supplementary Table 4, where, for two central parameters, the occupancy and height of the Pt_{ex} atoms, and three characteristic potentials, 1.07, 1.12 and 1.17 V, the results of the best fits obtained by four different surface models are given.

Computational methods. The DFT calculations were carried out using the Vienna ab initio simulation code, version 5.3.5-avx⁴⁹. The projector augmented-wave method⁵⁰ was used to describe the interaction between the core electrons and the valence electron density, described by means of a plane wave basis set and the Perdew–Burke–Ernzerhof (PBE) exchange–correlation functional⁵¹. In the optimization, we used a plane wave cutoff of 450 eV, the convergence criterion for the atomic forces was 0.05 eV \AA^{-1} and dipole corrections were applied between periodically repeated images along the z axis. In the four-layer-thick (3×3) Pt(111) and (3×3) Pt(100) slabs, the two topmost layers and the adsorbates were fully relaxed, whereas the two bottommost layers were fixed. For both slabs, the k -point sampling was $(4 \times 4 \times 1)$. H_2 and H_2O were simulated in cubic boxes with a volume of 3375 \AA^3 , sampling the gamma point only. The free energies (G) were approximated as: $G = E^{\text{DFT}} + \text{ZPE} - \text{TS} + G^{\text{olv}}$. E^{DFT} is the total energy calculated with DFT. The zero-point energy (ZPE) and vibrational entropy (TS^{olv}) corrections for the adsorbed species were calculated within the harmonic oscillator approximation, whereas for H_2 and H_2O , the values were taken from

thermodynamic tables (Supplementary Tables 5 and 6)⁵². Solvation contributions to the adsorption energies (G^{olv}) of $\text{H}_2\text{O}_{\text{ads}}$ and OH_{ads} were taken from previous studies^{53,54}. Proton and electron transfer were modelled using the computational hydrogen electrode⁵⁵. The Pourbaix diagrams of Pt(111) and Pt(100) presented in Extended Data Fig. 5 were built following the methodology described previously⁵⁶.

The energetics of Pt dissolution as Pt^{2+} and PtOH^+ were evaluated on the basis of the experimental standard dissolution potential of Pt of 1.18 V and that of the reaction $\text{PtOH}^+ + \text{H}^+ + 2\text{e}^- \rightarrow \text{Pt} + \text{H}_2\text{O}$, which is 1.20 V (ref. 52). From these two calculations, we concluded that Pt^{2+} is slightly favoured over PtOH^+ , thermodynamically speaking. In addition, we note that the cohesive energy of bulk Pt provided by the PBE exchange-correlation functional is 5.54 eV, whereas experimentally it was determined to be 5.87 eV (ref. 57). Thus, a correction of 0.33 eV needs to be applied.

The calculated Pourbaix diagrams (Extended Data Fig. 5) show that O_{ads} is more strongly adsorbed on Pt(111) compared with on Pt(100) at the same coverage and adsorbs at twofold bridge sites on Pt(100) and at threefold fcc hollow sites on Pt(111) (Supplementary Table 5). At a given potential, the oxygen coverage (θ_{O}) is typically larger on Pt(100) than on Pt(111) due to lower lateral repulsion, corresponding well with previous calculations^{56,58}.

Data availability

The raw X-ray data as well as the atomic coordinates of the optimized computational models have been deposited in the repository <https://doi.org/10.5281/zenodo.3937672>. All other data supporting the findings of this study are available within the article and its Supplementary Information, or from the corresponding author upon reasonable request. Source data are provided with this paper.

Code availability

The custom software for the analysis of the CTR data and the custom BINoculars backend for HESXRD structure factor determination are deposited in the repository <https://doi.org/10.5281/zenodo.3941003>. All other software used for this study is publicly available or can be obtained from the corresponding author upon reasonable request.

Received: 13 February 2020; Accepted: 18 July 2020;

Published online: 24 August 2020

References

- Meier, J. C. et al. Design criteria for stable Pt/C fuel cell catalysts. *Beilstein J. Nanotech.* **5**, 44–67 (2014).
- Climent, V. & Felii, J. M. Thirty years of platinum single crystal electrochemistry. *J. Solid State Electrochem.* **15**, 1297–1315 (2011).
- Conway, B. E. & Jerkiewicz, G. Surface orientation dependence of oxide film growth at platinum single crystals. *J. Electroanal. Chem.* **339**, 123–146 (1992).
- You, H., Zurawski, D. J., Nagy, Z. & Yonco, R. M. *In-situ* x-ray reflectivity study of incipient oxidation of Pt(111) surface in electrolyte solutions. *J. Chem. Phys.* **100**, 4699–4702 (1994).
- Tidswell, I., Markovic, N. & Ross, P. Potential dependent surface structure of the Pt(1 1 1) electrolyte interface. *J. Electroanal. Chem.* **376**, 119–126 (1994).
- Wakisaka, M., Udagawa, Y., Suzuki, H., Uchida, H. & Watanabe, M. Structural effects on the surface oxidation processes at Pt single-crystal electrodes studied by X-ray photoelectron spectroscopy. *Energy Environ. Sci.* **4**, 1662–1666 (2011).
- Gómez-Marín, A. M. & Felii, J. M. Oxide growth dynamics at Pt(111) in absence of specific adsorption: a mechanistic study. *Electrochim. Acta* **104**, 367–377 (2013).
- Tanaka, H. et al. Infrared reflection absorption spectroscopy of OH adsorption on the low index planes of Pt. *Electrocatalysis* **6**, 295–299 (2014).
- Sugimura, F., Nakamura, M. & Hoshi, N. The oxygen reduction reaction on kinked stepped surfaces of Pt. *Electrocatalysis* **8**, 46–50 (2016).
- Huang, Y.-F., Kooyman, P. J. & Koper, M. T. M. Intermediate stages of electrochemical oxidation of single-crystalline platinum revealed by in situ Raman spectroscopy. *Nat. Commun.* **7**, 12440 (2016).
- Sugimura, F. et al. In situ observation of Pt oxides on the low index planes of Pt using surface enhanced Raman spectroscopy. *Phys. Chem. Chem. Phys.* **19**, 27570–27579 (2017).
- Furuya, N. & Shibata, M. Structural changes at various Pt single crystal surfaces with potential cycles in acidic and alkaline solutions. *J. Electroanal. Chem.* **467**, 85–91 (1999).
- Itaya, K., Sugawara, S., Sashikata, K. & Furuya, N. In situ scanning tunneling microscopy of platinum (111) surface with the observation of monatomic steps. *J. Vac. Sci. Technol. A* **8**, 515–519 (1990).
- Lopes, P. P. et al. Relationships between atomic level surface structure and stability/activity of platinum surface atoms in aqueous environments. *ACS Catal.* **6**, 2536–2544 (2016).
- Lopes, P. P. et al. Dynamics of electrochemical Pt dissolution at atomic and molecular levels. *J. Electroanal. Chem.* **819**, 123–129 (2018).
- Sandbeck, D. J. et al. Dissolution of platinum single crystals in acidic medium. *ChemPhysChem* **20**, 2997–3003 (2019).
- Ruge, M. et al. Structural reorganization of Pt(111) electrodes by electrochemical oxidation and reduction. *J. Am. Chem. Soc.* **139**, 4532–4539 (2017).
- Ruge, M. et al. Electrochemical oxidation of smooth and nanoscale rough Pt(111): an in situ surface X-ray scattering study. *J. Electrochem. Soc.* **164**, H608–H614 (2017).
- Jacobse, L., Huang, Y.-F., Koper, M. T. M. & Rost, M. J. Correlation of surface site formation to nanoisland growth in the electrochemical roughening of Pt(111). *Nat. Mater.* **17**, 277–282 (2018).
- Arulmozhi, N., Esau, D., Lamsal, R. P., Beauchemin, D. & Jerkiewicz, G. Structural transformation of monocrystalline platinum electrodes upon electro-oxidation and electro-dissolution. *ACS Catal.* **8**, 6426–6439 (2018).
- Topalov, A. A. et al. Dissolution of platinum: limits for the deployment of electrochemical energy conversion? *Angew. Chem. Int. Ed.* **51**, 12613–12615 (2012).
- Gómez-Marín, A. M. & Felii, J. M. Pt(111) surface disorder kinetics in perchloric acid solutions and the influence of specific anion adsorption. *Electrochim. Acta* **82**, 558–569 (2012).
- Drnec, J. et al. Initial stages of Pt(111) electrooxidation: dynamic and structural studies by surface X-ray diffraction. *Electrochim. Acta* **224**, 220–227 (2017).
- Drnec, J., Harrington, D. & Magnussen, O. Electrooxidation of Pt(111) in acid solution. *Curr. Opin. Electrochem.* **4**, 69–75 (2017).
- Liu, Y., Barbour, A., Komanicky, V. & You, H. X-ray crystal truncation rod studies of surface oxidation and reduction on Pt(111). *J. Phys. Chem. C* **120**, 16174–16178 (2016).
- Fantauzzi, D., Mueller, J. E., Sabo, L., van Duin, A. C. T. & Jacob, T. Surface buckling and subsurface oxygen: atomistic insights into the surface oxidation of Pt(111). *ChemPhysChem* **16**, 2797–2802 (2015).
- Eslamibidgoli, M. J. & Eikerling, M. H. Atomistic mechanism of Pt extraction at oxidized surfaces: insights from DFT. *Electrocatalysis* **7**, 345–354 (2016).
- Gu, Z. & Balbuena, P. B. Chemical environment effects on the atomic oxygen absorption into Pt(111) subsurfaces. *J. Phys. Chem. C* **111**, 17388–17396 (2007).
- Rodes, A., Zamakhchari, M. A., El Achi, K. & Clavilier, J. Electrochemical behaviour of Pt(100) in various acidic media: part I. On a new voltammetric profile of Pt(100) in perchloric acid and effects of surface defects. *J. Electroanal. Chem.* **305**, 115–129 (1991).
- Gustafson, J. et al. High-energy surface X-ray diffraction for fast surface structure determination. *Science* **343**, 758–761 (2014).
- Devarajan, S. P., Hinojosa, J. A. & Weaver, J. F. STM study of high-coverage structures of atomic oxygen on Pt(1 1 1): p(2 × 1) and Pt oxide chain structures. *Surf. Sci.* **602**, 3116–3124 (2008).
- Van Spronsen, M. A., Frenken, J. W. & Groot, I. M. Observing the oxidation of platinum. *Nat. Commun.* **8**, 429 (2017).
- Xing, L., Jerkiewicz, G. & Beauchemin, D. Ion exchange chromatography coupled to inductively coupled plasma mass spectrometry for the study of Pt electro-dissolution. *Anal. Chim. Acta* **785**, 16–21 (2013).
- Cherevko, S., Kulyk, N. & Mayrhofer, K. J. Durability of platinum-based fuel cell electrocatalysts: dissolution of bulk and nanoscale platinum. *Nano Energy* **29**, 275–298 (2016).
- Cherevko, S., Topalov, A. A., Zeradjani, A. R., Keeley, G. P. & Mayrhofer, K. J. Temperature-dependent dissolution of polycrystalline platinum in sulfuric acid electrolyte. *Electrocatalysis* **5**, 235–240 (2014).
- Geiger, S. *Stability Investigations of Iridium-Based Catalysts Towards Acidic Water Splitting*. Dissertation, Ruhr-Universität Bochum (2018).
- Lamsal, R. P., Jerkiewicz, G. & Beauchemin, D. Enhancement of the capabilities of inductively coupled plasma mass spectrometry using monosegmented flow analysis. *Anal. Chem.* **90**, 13842–13847 (2018).
- Sandbeck, D. J. S. *On the Dissolution of Platinum: From Fundamental to Advanced Catalytic Materials*. Dissertation, Friedrich-Alexander-Universität Erlangen-Nürnberg (2020).
- Magnussen, O. M., Krug, K., Ayyad, A. H. & Stettner, J. In situ diffraction studies of electrode surface structure during gold electrodeposition. *Electrochim. Acta* **53**, 3449–3458 (2008).
- Drnec, J. et al. Pt oxide and oxygen reduction at Pt(111) studied by surface X-ray diffraction. *Electrochim. Commun.* **84**, 50–52 (2017).
- Ashiotis, G. et al. The fast azimuthal integration Python library: PyFAI. *J. Appl. Crystallogr.* **48**, 510–519 (2015).
- Busing, W. R. & Levy, H. A. Angle calculations for 3- and 4-circle X-ray and neutron diffractometers. *Acta Crystallogr.* **22**, 457–464 (1967).
- Wang, J., Ocko, B., Davenport, A. & Isaacs, H. In situ x-ray-diffraction and -reflectivity studies of the Au(111)/electrolyte interface: Reconstruction and anion adsorption. *Phys. Rev. B* **46**, 10321–10338 (1992).

44. Roobol, S., Onderwaater, W., Drnec, J., Felici, R. & Frenken, J. BINoculars: data reduction and analysis software for two-dimensional detectors in surface X-ray diffraction. *J. Appl. Crystallogr.* **48**, 1324–1329 (2015).
45. Vlieg, E. Integrated intensities using a six-circle surface X-ray diffractometer. *J. Appl. Crystallogr.* **30**, 532–543 (1997).
46. Drnec, J. et al. Integration techniques for surface X-ray diffraction data obtained with a two-dimensional detector. *J. Appl. Crystallogr.* **47**, 365–377 (2014).
47. Feidenhans'l, R. Surface structure determination by X-ray diffraction. *Surf. Sci. Rep.* **10**, 105–188 (1989).
48. Press, W. H., Teukolsky, S. A., Vetterling, W. T. & Flannery, B. P. *Numerical Recipes in C: The Art of Scientific Computing* 2nd edn, (Cambridge Univ. Press, 1992).
49. Kresse, G. & Furthmüller, J. Efficient iterative schemes for ab initio total-energy calculations using a plane-wave basis set. *Phys. Rev. B* **54**, 11169–11186 (1996).
50. Kresse, G. & Joubert, D. From ultrasoft pseudopotentials to the projector augmented-wave method. *Phys. Rev. B* **59**, 1758–1775 (1999).
51. Perdew, J. P., Burke, K. & Ernzerhof, M. Generalized gradient approximation made simple. *Phys. Rev. Lett.* **77**, 3865–3868 (1996).
52. Lide, D. R. (ed) *CRC Handbook of Chemistry and Physics* (CRC Press, 2005).
53. Calle-Vallejo, F., de Morais, R., Illas, F., Loffreda, D. & Sautet, P. Affordable estimation of solvation contributions to the adsorption energies of oxygenates on metal nanoparticles. *J. Phys. Chem. C* **123**, 5578–5582 (2019).
54. He, Z.-D., Hanselman, S., Chen, Y.-X., Koper, M. T. M. & Calle-Vallejo, F. Importance of solvation for the accurate prediction of oxygen reduction activities of Pt-based electrocatalysts. *J. Phys. Chem. Lett.* **8**, 2243–2246 (2017).
55. Nørskov, J. K. et al. Origin of the overpotential for oxygen reduction at a fuel-cell cathode. *J. Phys. Chem. B* **108**, 17886–17892 (2004).
56. Hansen, H. A., Rossmeis, J. & Nørskov, J. K. Surface Pourbaix diagrams and oxygen reduction activity of Pt, Ag and Ni(111) surfaces studied by DFT. *Phys. Chem. Chem. Phys.* **10**, 3722–3730 (2008).
57. Janthon, P. et al. Bulk properties of transition metals: a challenge for the design of universal density functionals. *J. Chem. Theory Comput.* **10**, 3832–3839 (2014).
58. Bizzotto, F. et al. Examining the structure sensitivity of the oxygen evolution reaction on Pt single-crystal electrodes: a combined experimental and theoretical study. *ChemPhysChem* **20**, 3154–3162 (2019).

Acknowledgements

We acknowledge the European Synchrotron Radiation Facility for provision of SXRD facilities, and H. Isern and T. Dufrane for their help with the SXRD experiments. Funding is acknowledged from the NSERC (grant no. RGPIN-2017-04045) and Deutsche Forschungsgemeinschaft (grant nos. MA 1618/23 and CH 1763/5-1). F.C.-V acknowledges funding from Spanish MICIUN RTI2018-095460-B-I00 and María de Maeztu MDM-2017-0767 grants, and thanks RES for supercomputing time at SCAYLE (projects QS-2019-3-0018, QS-2019-2-0023, and QCM-2019-1-0034) and MareNostrum (project QS-2020-1-0012). The use of supercomputing facilities at SURFsara was sponsored by NWO Physical Sciences, with financial support by NWO.

Author contributions

T.F., J.D., N.S., M.R., D.A.H. and O.M.M. designed and performed the SXRD experiments. T.F. analysed the SXRD data. D.J.S.S. and S.C. designed and performed the SFC-ICP-MS experiments. D.J.S.S. analysed the SFC-ICP-MS data. F.C.-V. performed the DFT calculations. T.F., J.D., D.A.H., D.J.S.S., S.C., F.C.-V. and O.M.M. were involved in the interpretation of the results and prepared the manuscript.

Competing interests

The authors declare no competing interests.

Additional information

Extended data is available for this paper at <https://doi.org/10.1038/s41929-020-0497-y>.

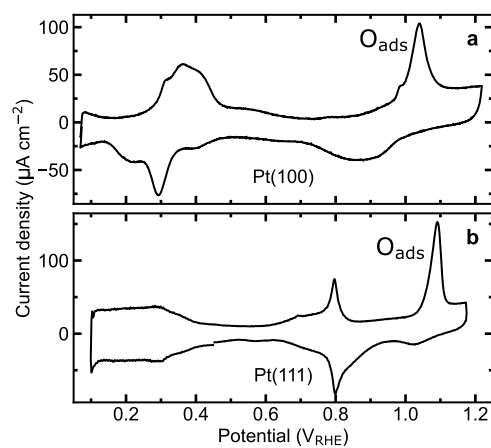
Supplementary information is available for this paper at <https://doi.org/10.1038/s41929-020-0497-y>.

Correspondence and requests for materials should be addressed to O.M.M.

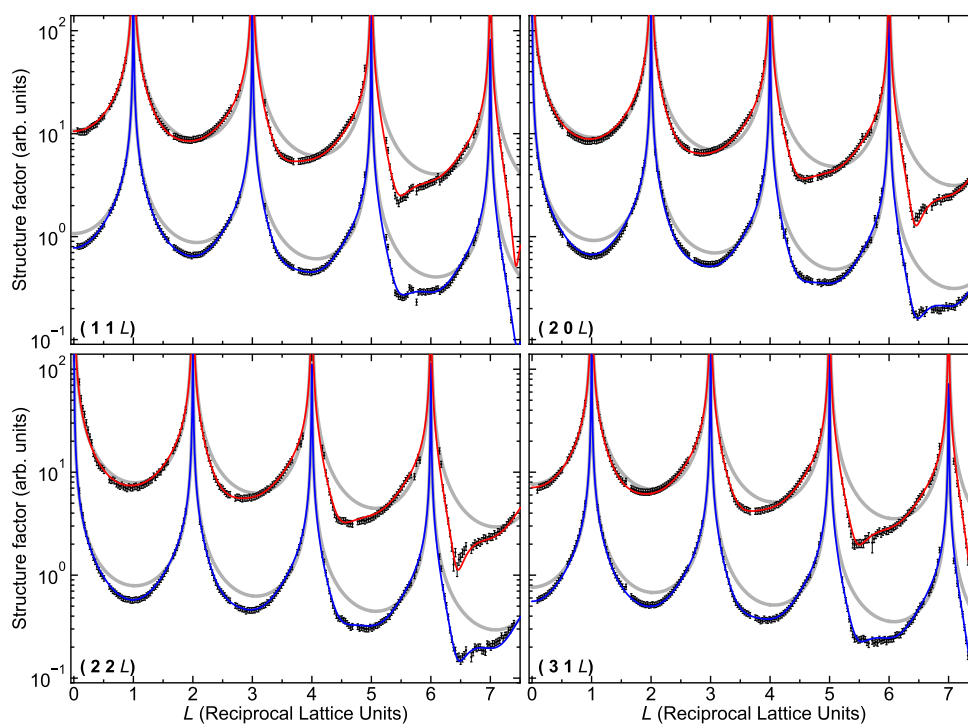
Reprints and permissions information is available at www.nature.com/reprints.

Publisher's note Springer Nature remains neutral with regard to jurisdictional claims in published maps and institutional affiliations.

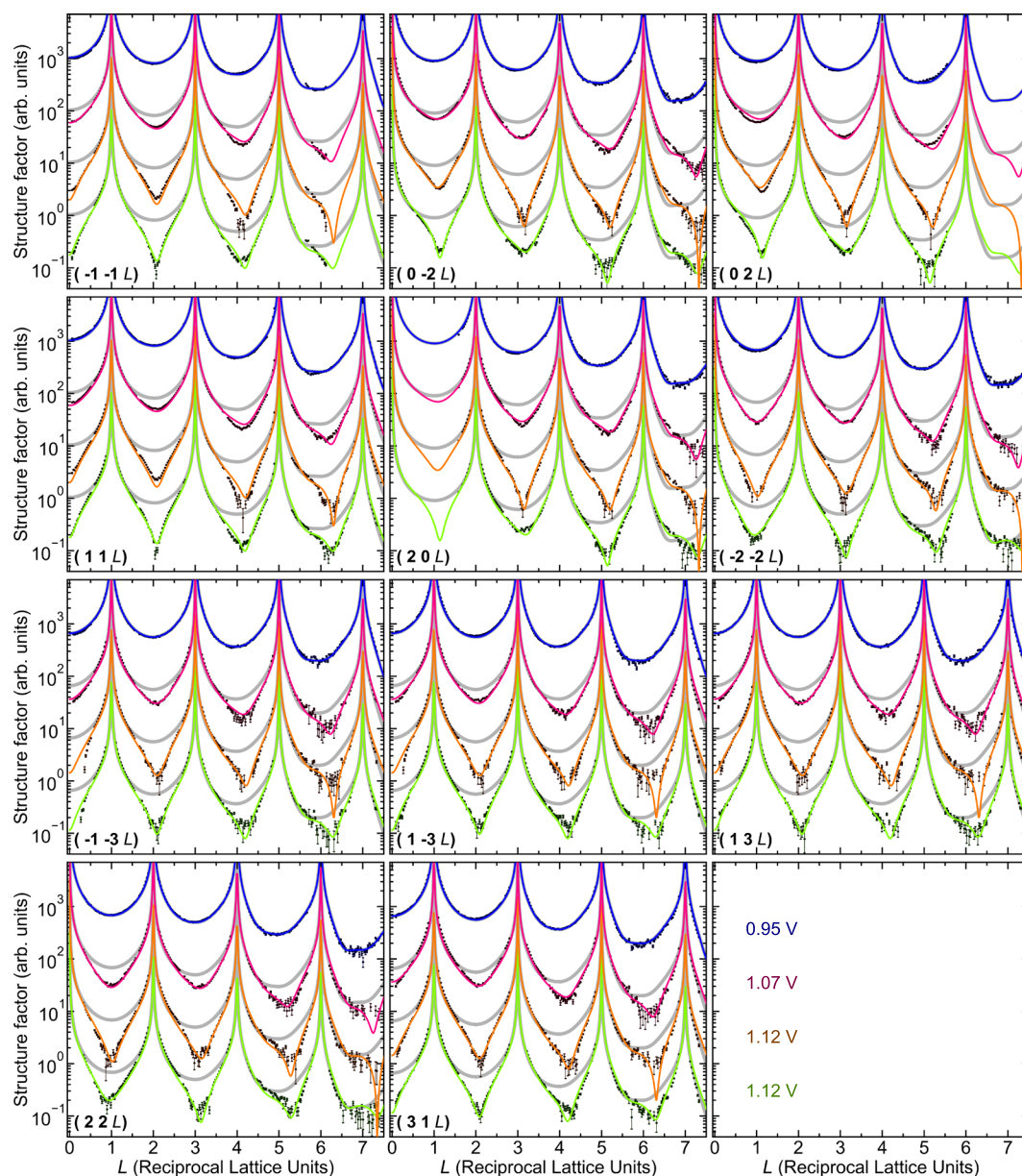
© The Author(s), under exclusive licence to Springer Nature Limited 2020



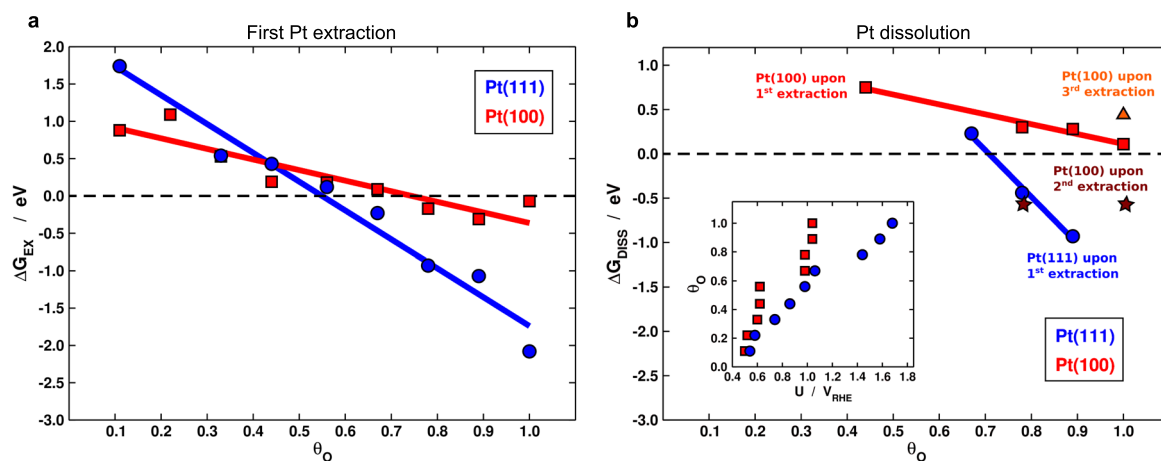
Extended Data Fig. 1 | Cyclic voltammograms measured in the electrochemical cell used for the Surface X-ray Diffraction measurements. Cyclic voltammograms of (a) Pt(100) and (b) Pt(111) in 0.1 M HClO_4 with a scan rate of 50 mV/s.



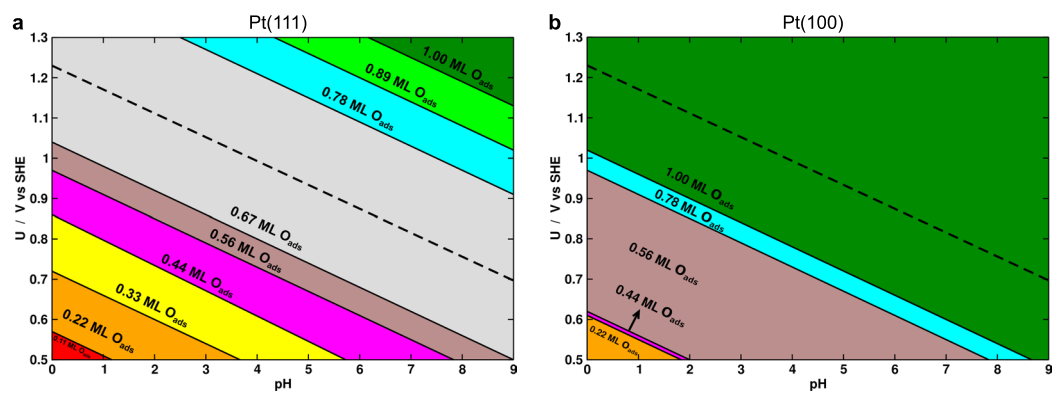
Extended Data Fig. 2 | Crystal truncation rods of Pt(100) at 0.12 V prior to surface oxidation and after oxide reduction. Crystal truncation rods (CTR) of the pristine Pt(100) surface after sample preparation and the CTRs of the roughened Pt(100) surface after oxide formation at 1.17 V and subsequent oxide reduction at 0.12 V. The grey lines indicate the CTRs of a bulk terminated Pt(100) surface. The decrease of the CTR structure factor after surface oxidation can be attributed to the formation of adatoms Pt_{ad} and vacancies in the Pt₁ layer. Best fits with a quantitative model (solid blue line) that includes these surface defects result in a Pt_{ad} coverage of 0.07 ML.



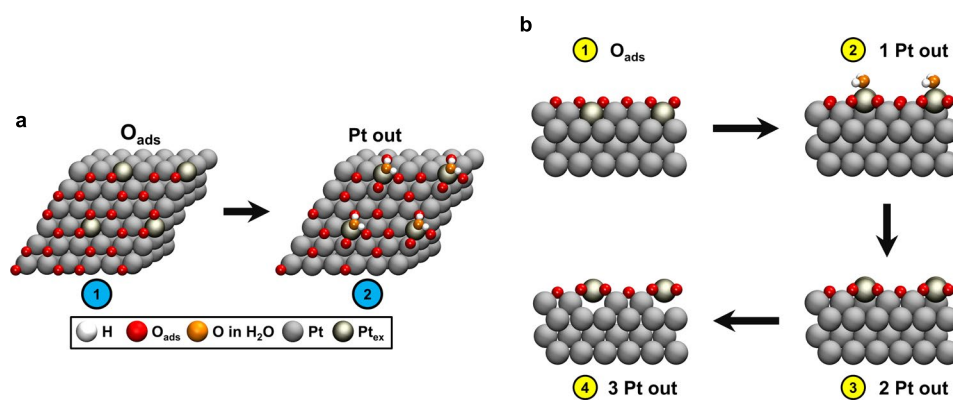
Extended Data Fig. 3 | Crystal truncation rods (CTR) and corresponding CTR fits of Pt(100) close to and in the region of oxide formation. CTRs of Pt(100) at a potential slightly negative (0.95 V) and three potentials positive (1.07, 1.12 and 1.17 V) of the O_{ads} peak in the cyclic voltammogram (Fig. 1b, Extended Data Fig. 1). Solid lines are the corresponding CTR fits. The CTRs for the different potentials are offset to each other by a factor 10 and shown together with the CTR fits of the smooth surface at 0.95 V (grey lines). Details on the CTR fits are given in the Supplementary Note 3 and the corresponding structural parameters are given in Supplementary Table 4.



Extended Data Fig. 4 | Gibbs energy for the first Pt extraction and the subsequent dissolution of Pt. (a) Oxygen coverage θ_o dependent Gibbs energy ΔG for the extraction of the first atom on Pt(111) and Pt(100). **(b)** ΔG for the dissolution of the extracted atom after first extraction on Pt(111) and first, second and third extraction on Pt(100). The correspondence between the oxygen coverage θ_o and potential U is in the inset of **(b)**.



Extended Data Fig. 5 | Pourbaix diagrams for O adsorption. Pourbaix diagram of (a) Pt(111) and (b) Pt(100). The dashed line represents the oxygen reduction reaction ($O_2 + 4(H^+ + e^-) \rightarrow 2H_2O$).



Extended Data Fig. 6 | Additional views of the lowest-energy structures in the process of Pt extraction. (a) Top view of the Pt extraction process on Pt(111). **(b)** Side view of the Pt extraction process on Pt(100).